GDCh

Research Article

Angewandte
Chemie
International Edition
www.angewandte.org

Nitrogen Reduction

Modulating the Leverage Relationship in Nitrogen Fixation Through Hydrogen-Bond-Regulated Proton Transfer

Shaoce Zhang[+], Hu Hong[+], Rong Zhang, Zhiquan Wei, Yiqiao Wang, Dong Chen, Chuan Li, Pei Li, Huilin Cui, Yue Hou, Shengnan Wang, Johnny C. Ho, Ying Guo,* Zhaodong Huang, and Chunyi Zhi*

Abstract: In the electrochemical nitrogen reduction reaction (NRR), a leverage relationship exists between NH_3-producing activity and selectivity because of the competing hydrogen evolution reaction (HER), which means that high activity with strong protons adsorption causes low product selectivity. Herein, we design a novel metal-organic hydrogen bonding framework (MOHBF) material to modulate this leverage relationship by a hydrogen-bond-regulated proton transfer pathway. The MOHBF material was composited with reduced graphene oxide (rGO) to form a $Ni-N_2O_2$ molecular catalyst ($Ni-N_2O_2$/rGO). The unique structure of O atoms in Ni-O-C and N-O-H could form hydrogen bonds with H_2O molecules to interfere with protons being directly adsorbed onto Ni active sites, thus regulating the proton transfer mechanism and slowing the HER kinetics, thereby modulating the leverage relationship. Moreover, this catalyst has abundant Ni-single-atom sites enriched with Ni-N/O coordination, conducive to the adsorption and activation of N_2. The $Ni-N_2O_2$/rGO exhibits simultaneously enhanced activity and selectivity of NH_3 production with a maximum NH_3 yield rate of $209.7\ \mu g\,h^{-1}\,mg_{cat.}^{-1}$ and a Faradaic efficiency of 45.7%, outperforming other reported single-atom NRR catalysts.

Introduction

Ammonia (NH_3) is an essential feedstock in fertilizer and medicine production and a promising energy carrier because of its high hydrogen storage capacity.[1] Industrial NH_3 synthesis is mainly conducted using the conventional energy-intensive Haber-Bosch approach, which requires high temperature and pressure owing to the large dissociation energy of nitrogen (N_2), resulting in substantial consumption of fossil fuel and high greenhouse gas emissions.[2] Next-generation technologies for synthesizing NH_3 must be developed to reduce the associated energy consumption and promote carbon neutrality.[3] The electrochemical N_2 reduction reaction (NRR) conducted under ambient conditions using a clean proton source, namely H_2O, has become an attractive alternative for synthesizing NH_3.[4] Unfortunately, the slow kinetics of the NRR and the competing hydrogen evolution reaction (HER) severely limit activity and selectivity during the NRR. This problem might be solved by using high-efficiency electrocatalysts.[5]

In general, both activity and selectivity are crucial considerations when a state-of-the-art catalyst is designed for the NRR;[6] however, a leverage relationship often exists between them.[7] To ensure high NRR selectivity for a specific active site, the active site must be designed to have robust N_2 adsorption capability,[8] and thus relatively weak proton adsorption. Such an active site hinders hydrogenation and leads to sluggish N_2-to-NH_3 conversion in the NRR, hence resulting in poor activity (Figure 1a). Conversely, if the local environment of the active site has sufficient protons for six proton-coupled electron transfer reactions to occur

---

[*] S. Zhang,[+] H. Hong,[+] R. Zhang, Z. Wei, Y. Wang, D. Chen, C. Li,
P. Li, H. Cui, Y. Hou, Dr. S. Wang, Prof. J. C. Ho, Dr. Z. Huang,
Prof. C. Zhi
Department of Materials Science and Engineering, City University
of Hong Kong, 83 Tat Chee Avenue, Kowloon, Hong Kong 999077,
China.
E-mail: cy.zhi@cityu.edu.hk

S. Zhang,[+] R. Zhang, P. Li, H. Cui, Y. Hou, Dr. Z. Huang, Prof. C. Zhi
Hong Kong Center for Cerebro-Cardiovascular Health Engineering
(COCHE), Shatin, NT, HKSAR, China.

Dr. Y. Guo
College of Materials Science and Engineering, Shenzhen University,
518061, Shenzhen, China.
E-mail: yingguo@szu.edu.cn

Prof. C. Zhi
Centre for Functional Photonics, City University of Hong Kong,
Kowloon, Hong Kong.

Prof. C. Zhi
Hong Kong Institute for Clean Energy, City University of Hong
Kong, Kowloon 999077, Hong Kong.

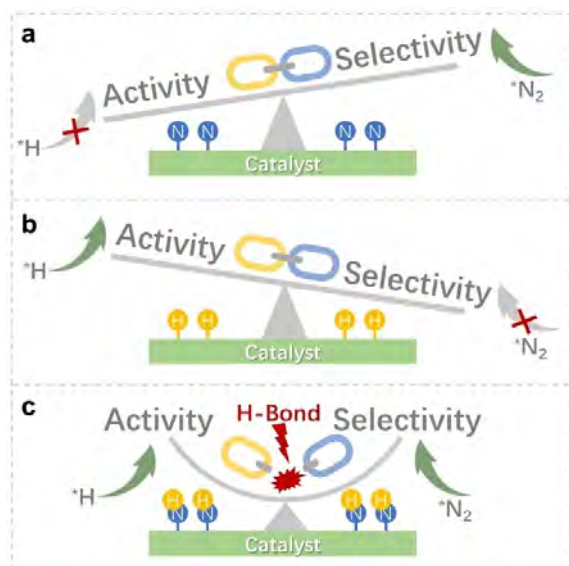[+] These authors contributed equally to this work.

Figure 1. Schematic diagram of the leverage relationship. a,b) Leverage relationship of catalysts with a) low activity and high selectivity and b) high activity and low selectivity. c) The modulated leverage relationship between activity and selectivity in the NRR.

rapidly,[9] the excessive proton accessibility contributes to a strongly competing HER.[7,10] This phenomenon causes high activity but low selectivity (Figure 1b). Such a leverage relationship poses a challenge to simultaneously improving selectivity and activity.

Exploring how the activity of the competing HER can be suppressed as much as possible while sufficient protons are supplied is critical. Because of their highly exposed active sites and unique quantum size effects, transition metal (TM) single-atom (SA) catalysts exhibit high potential for the NRR.[11] These catalysts have both occupied and unoccupied d-orbitals; thus, they can donate electrons to the empty π^* orbital of N_2 and accept the lone-pair σ electrons of N_2, thereby effectively activating N_2 molecules.[12] However, the electrons in the d-orbitals of TM SA catalysts can also create strong metal-H bonds, which cause the competing HER to be more kinetically dominant than the NRR, leading to poor selectivity for NH_3 synthesis.[7] A rational strategy for the design of TM SA catalysts is required to modulate the leverage relationship. A hydrogen bond between H_2O molecules is a typical dipole-dipole interaction.[13] If such a bond can be incorporated into TM SA catalysts, the motion of H_2O molecules in aqueous solutions may be effectively inhibited, thereby modulating the leverage relationship and enhancing the performance of the NRR (Figure 1c); a suitable approach for this purpose has not yet been reported.

In this study, we designed a novel Ni SA molecular catalyst with a metal-organic hydrogen bonding framework (MOHBF), and based on this framework, we fabricated a reduced graphene oxide (rGO)-supported $Ni-N_2O_2$ molecular catalyst ($Ni-N_2O_2$/rGO). Ni with a unique nearly full d orbital makes it promising in NRR. The Ni SA centers in $Ni-N_2O_2$/rGO, which have asymmetric O/N coordination,

exhibit robust ability in polarizing and activating N_2 molecules. More importantly, the unique structure of O atoms in Ni-O-C and N-O-H can form hydrogen bonds with H_2O molecules and thus weaken the activity of these H_2O molecules, thereby effectively regulating the migration of protons and suppressing the parasitic HER. Consequently, the proposed molecular catalyst enhance both activity and selectivity, with its NH_3 yield rate being 209.7 $\mu g\,h^{-1}\,mg_{cat.}^{-1}$ and Faradaic efficiency (FE) being 45.7% at -0.30 V vs. reversible hydrogen electrode (RHE), which outperforms other reported SA NRR catalysts.

Results and Discussion

We first used $Ni(NO_3)_2\cdot6H_2O$ and salicylhydroxamic acid as raw materials to prepare MOHBF (Figure S1). The scanning electron microscopy (SEM) image indicated that the framework comprised nanorods with a smooth surface and uniform size (Figure S2). The Rietveld refinement of X-ray diffraction (XRD) pattern (Figure S3) revealed that the material was monoclinic with the $P2_1/c$ space group (Table S1). The X-ray photoelectron spectroscopy (XPS) results suggested the coexistence of Ni–O (peak at 532.6 eV in the high-resolution O 1s spectra) and Ni–N (peak at 399.0 eV in the high-resolution N 1s spectra) bonds (Figure S4).[14] The Fourier transform infrared spectroscopy (FTIR) pattern (Figure S5) contained the characteristic peaks of the C=N (1625 cm^{-1}), C=C (1583 and 1539 cm^{-1}), O–H (1413 cm^{-1}), C–O (1306 cm^{-1}), and C–H (1286 and 1147 cm^{-1}) bonds.[15] The aforementioned results indicated the successful synthesis of the MOHBF. We calculated the electrostatic potential (ESP) of the MOHBF to study its charge distribution. As shown in Figure 2a, the O sites in Ni-O-C and N-O-H in the molecular monomers of the MOHBF had a more negative ESP than the sites of other elements, which favored the formation of hydrogen bonds with H_2O molecules near the Ni active sites. This finding was verified by the reduced density gradient (RDG) isosurface map (Figure S6) and corresponding scatter diagram (Figure 2b), in which the blue peaks located between -0.03 and -0.04 a.u., demonstrating the ability of intramolecular O sites to form hydrogen bonds.

Subsequently, Ni K-edge X-ray absorption fine structure (XAFS) spectroscopy was performed to gain a deeper understanding of the chemical state and local coordination environment of Ni sites within the MOHBF catalyst. The X-ray absorption near-edge structure (XANES) spectra in Figure 2c indicated that the valence state of Ni fell between 0 for Ni foil and $+2$ for NiO and more closely to a $+2$ oxidation state. The Fourier-transformed extended XAFS (FT-EXAFS) curve of the MOHBF (Figure 2d) contained a prominent signal centered at 1.58 Å, between the peaks corresponding to Ni–N (1.49 Å) and Ni–O (1.70 Å) bonds, which suggested that the existence of Ni–N or Ni–O bonds, while no scattering peaks corresponded to the Ni–Ni coordination. This confirmed that Ni was atomically dispersed in the MOHBF. The extended XAFS (EXAFS) spectra fitting was performed in R and k spaces to
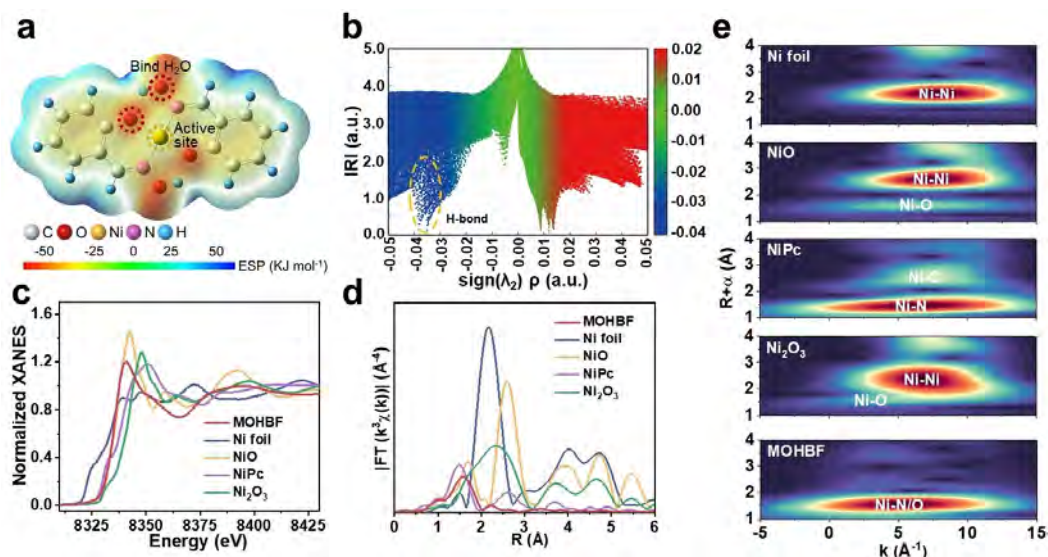
Figure 2. Structural characterization and performance evaluation of the designed MOHBF. a) The ESP diagram and b) RDG scatter diagram for Ni-N_2O_2 in the MOHBF. c) Ni K-edge XANES, d) FT-EXAFS, and e) WT-EXAFS spectra of MOHBF, Ni foil, NiO, NiPc, and Ni_2O_3.

investigate the coordination configuration of Ni atoms (Figure S7). The fitting results revealed that all fitted curves were consistent with the experimental results and that the Ni sites in the MOHBF were coordinated with N and O atoms (Table S2), which had average bonds of 1.99 Å for Ni–N and 2.08 Å for Ni–O. In contrast to the wavelet-transform EXAFS (WT-EXAFS) patterns of Ni foil, NiO, and Ni_2O_3, that of the MOHBF (Figure 2e) did not contain a WT signal for Ni–Ni bonds, which suggested the atomic dispersion of Ni sites in the MOHBF.

The NRR performance of the MOHBF was evaluated in 0.1 M phosphate buffer solution (PBS) by using an H-type electrolytic cell, and the measured potential was calibrated using an RHE. The linear sweep voltammetry (LSV) curves of the MOHBF (Figure S8) were obtained in N_2- or Ar-saturated 0.1 M PBS. The current density under N_2 conditions was higher than that under Ar conditions within the potential range, which revealed that the MOHBF was active in the NRR. The indophenol blue method (Figure S9) and Watt-Chrisp method (Figure S10) were used to conduct quantitative detection for the electrolysis product NH_3 and the possible by-product N_2H_4 in the electrolyte after a chronoamperometry test (Figure S11). Negligible quantities of N_2H_4 were collected at all potentials (Figure S12). As shown in Figure S13, the NH_3 yield rate and FE increased with negatively shifted potential, reaching 32.0 $\mu g\,h^{-1}\,mg_{cat.}^{-1}$ and 10.5 % at −0.3 V vs. RHE, respectively. Nevertheless, the electrocatalytic NRR performance of the MOHBF was unsatisfactory because of the framework's one-dimensional nanorod structure (Figure S2), which may hamper the exposure of O sites, thus cannot form hydrogen bonds to modulate the leverage relationship during the NRR.

To fully utilize the potential of hydrogen bonds for modulating the leverage relationship and enhancing the NRR performance, the created MOHBF was optimized through a melting process, as illustrated in Figure 3a.

Specifically, MOHBF nanorods were melted into Ni-N_2O_2 molecules anchored on an NRR-inert rGO (Figure S14) substrate (Ni-N_2O_2/rGO) on the basis of thermogravimetry–differential scanning calorimetry (TG-DSC) curves (Figure S15). This process yielded a sheet-like composite structure (Figure S16). The energy-dispersive X-ray spectroscopy (EDS) mapping presented in Figure S17 revealed that Ni-N_2O_2 was uniformly distributed across the rGO substrate. The XAFS spectroscopy results for Ni-N_2O_2/rGO (Figure S18 and Table S2) confirmed that the coordination structure of Ni sites was unaffected by the melting process. Furthermore, Ni-N_2O_2 had a carbon ring that exhibited a high degree of conjugation with the rGO substrate, which was demonstrated by a comparative analysis of the surface potential through Kelvin probe force microscopy (KPFM) measurement performed before and after Ni-N_2O_2 loading (Figures 3b and S19). Density functional theory (DFT) calculations provided additional confirmation of π-π interactions in the Ni-N_2O_2/rGO composite (spikes between −0.01 and 0.00 a.u., Figure S20). Interactions in the out-of-plane direction promoted interfacial charge transfer, which considerably enhanced the conductivity of the catalyst.[16]

The catalysts with various Ni-N_2O_2 contents on the rGO substrate were fabricated to regulate the catalyst performance and investigate the mechanism of Ni-N_2O_2/rGO in the NRR. As illustrated in Figure S21, when N_2 was employed as the feed gas, the current density was positively correlated with Ni-N_2O_2 content. The heatmaps displayed in Figure 3c,d revealed that the FE and NH_3 yield rates of the catalysts with different Ni-N_2O_2 contents increased as the potential was negatively shifted and were highest at −0.3 V vs. RHE. Interestingly, as the Ni-N_2O_2 content was increased at each potential, the NH_3 yield rate showed an upward trend because of the more active sites, while the FE of NH_3 changed negligibly; however, both the FE and yield rate dropped sharply when the loading reached 80 wt % (Fig-
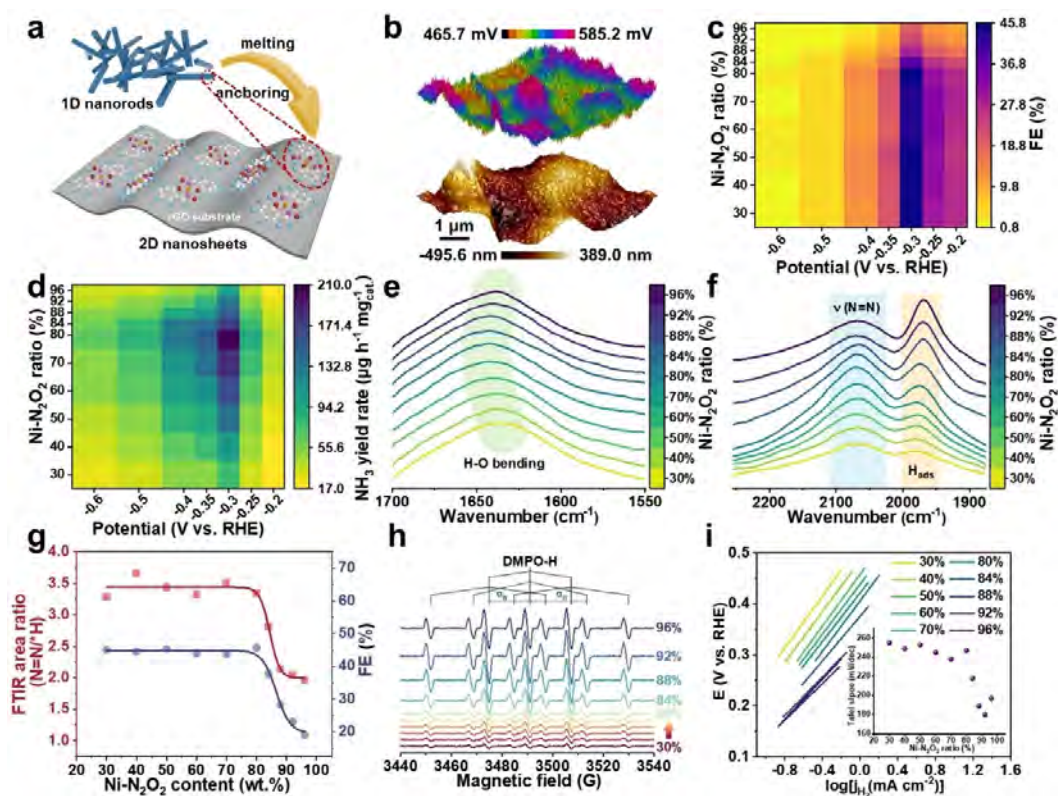
Figure 3. Performance of Ni-N$_2$O$_2$/rGO with various Ni-N$_2$O$_2$ contents in the NRR. a) Schematic diagram of Ni-N$_2$O$_2$/rGO preparation. b) AFM topography and KPFM image of Ni-N$_2$O$_2$/rGO. c) FE and d) NH$_3$ yield rate of Ni-N$_2$O$_2$/rGO with various Ni-N$_2$O$_2$ contents at each examined potential. ATR-FTIR spectroscopy results of the e) O—H bending mode and f) N=N stretching mode as well as adsorbed *H at −0.3 V vs. RHE for Ni-N$_2$O$_2$/rGO with differing Ni-N$_2$O$_2$ contents. g) $S_{N=N}/S_{*H}$ ratio based on f) and FE of NH$_3$ for various Ni-N$_2$O$_2$ contents. h) EPR results of DMPO-H at various Ni-N$_2$O$_2$ contents under hyperfine coupling constants of $a_N = 16.3$ G and $a_H = 22.5$ G. i) Tafel plots obtained in Ar atmosphere. Inset: Tafel slope values of catalysts with various Ni-N$_2$O$_2$ contents. In a), the yellow, red, blue, pink, and white spheres represent Ni, O, H, N, and C, respectively.

ure S22a,b). This trend was attributable to excessive Ni-N$_2$O$_2$ loading, causing the stacking of molecules and the interlinkage of intermolecular by hydrogen bonds, thus weakening the regulation of proton transfer. Then, the attenuated total reflection (ATR)-FTIR spectroscopy results of the catalysts with different Ni-N$_2$O$_2$ contents confirmed this finding. As shown in Figures 3e and S23, the O—H bending and stretching peaks shifted to higher wavenumbers when the Ni-N$_2$O$_2$ content increased, indicating that the activity of H$_2$O molecules was inhibited.[17] However, this inhibitory effect weakened as the Ni-N$_2$O$_2$ content increased beyond 80 wt%. Two characteristic signals were observed at 2071 and 1979 cm^{-1} in the ATR-FTIR spectroscopy results (Figure 3f); these signals corresponded to N=N stretching and *H adsorption at Ni sites, respectively. Gaussian fitting was conducted to calculate the $S_{N=N}/S_{*H}$ content ratio (Figure S24), and the curve of this ratio declined suddenly as the loading of Ni-N$_2$O$_2$ was increased beyond 80 wt%. These results are highly consistent with the trend obtained for the FE of NH$_3$ (Figure 3g). In the NRR, H$_2$O and N$_2$ compete for adsorption on Ni sites. O atoms in Ni-N$_2$O$_2$ can hydrogen-bind H$_2$O near a Ni site, thus hindering the direct adsorption of H$_2$O at the site and facilitating the adsorption of N$_2$ on the Ni site. Excessive Ni-N$_2$O$_2$ loading causes

molecules to connect through hydrogen bonds, weakening the control of H$_2$O molecules by hydrogen bonds near Ni sites and thereby enabling H$_2$O to adsorb on Ni sites quickly, which inhibits N$_2$ adsorption.

The aforementioned mechanism was confirmed through electron paramagnetic resonance (EPR) analysis in which 5,5-dimethyl-1-pyrroline-N-oxide (DMPO) was used as a trapping reagent. A chronoamperometry test for 10 minutes was conducted to achieve a dynamic balance between the production and consumption of active hydrogen. To eliminate the interference of rGO during the test, EPR was first performed using rGO as the working electrode in the chronoamperometry test; the resultant spectra contained no peaks (Figure S25). In the spectra obtained when Ni-N$_2$O$_2$/rGO was employed as the working electrode (Figure 3h), nine peaks with a 1:2 intensity ratio were obtained, which confirmed the presence of DMPO-H.[18] When the loading of Ni-N$_2$O$_2$ was not excessive, lower EPR signal intensity demonstrated greater consumption of active hydrogen in the NRR. When the loading of Ni-N$_2$O$_2$ exceeded 80 wt%, a large quantity of active hydrogen was competitively adsorbed at Ni sites because of the weakened regulation of hydrogen bonds; thus, the NRR was inhibited. Lower consumption of active hydrogen led to considerably stronger

EPR signals corresponding to DMPO-H. LSV tests involving various Ni-N$_2$O$_2$ contents were conducted in the Ar atmosphere (Figure S26). Electrochemical active surface area (ECSA) confirmed the more active sites with the increased Ni-N$_2$O$_2$ loading (Figures S27 and S28a),[19] which led to enhanced current density. The ECSA-normalized current densities (Figure S28b) remained stable as the Ni-N$_2$O$_2$ loading increased, indicating the catalytic activity for the HER was maintained. However, when the loading reached 80 wt %, the current densities exhibited an obvious increase, suggesting an enhancement in the HER activity. The Tafel plots (Figure 3i) also indicated that the hydrogen production barrier was negligibly affected by the Ni-N$_2$O$_2$ loading until it was increased beyond 80 wt %. The decreased Tafel slope (inset in Figure 3i) revealed the weakened hydrogen production barrier.[20] These phenomena were caused by the weakened ability of hydrogen bonds on the catalyst surface to control H$_2$O molecules near Ni sites. The aforementioned results indicate that hydrogen bonds interfered with the direct adsorption of protons on Ni sites, thus strengthening the barrier to the HER, thereby increasing selectivity for NH$_3$ generation.

Ni-N$_2$O$_2$/rGO with a Ni-N$_2$O$_2$ loading of 80 wt % (referred to as 80-Ni-N$_2$O$_2$/rGO) was selected for further investigation of the performance in the NRR. The LSV curves displayed in Figure S29 for 80-Ni-N$_2$O$_2$/rGO were obtained in N$_2$- or Ar-saturated 0.1 M PBS. Within the investigated potential range, the current density achieved with N$_2$-saturated PBS was higher than that obtained with Ar-saturated PBS, which highlighted the considerable activity of 80-Ni-N$_2$O$_2$/rGO in the NRR. The quantities of NH$_3$ product and potential N$_2$H$_4$ by-product were determined (Figure S30) after a chronoamperometry test (Figure S31). Notably, a negligible quantity of N$_2$H$_4$ was detected at all potentials (Figure S30b), which indicated the excellent NH$_3$ selectivity of 80-Ni-N$_2$O$_2$/rGO in the NRR. Figure 4a shows that the NH$_3$ yield rate and FE reached 209.7 µg h^{-1} mg$_{cat.}^{-1}$ and 45.7 % at -0.3 V vs. RHE. At potentials higher than -0.3 V, the NH$_3$ yield rate and FE decreased because of the strong competition of protons adsorbed on the active sites.[21] We also obtained LSV curves under different scan rates (Figure S32), which confirmed the presence of a diffusion-limitation feature. The magnetic stirring employed in the electrochemical measurements could effectively mitigate this influence. Figure 4b reveals that the performance of 80-Ni-N$_2$O$_2$/rGO was considerably superior to that of catalysts with other Ni-N$_2$O$_2$ loading ratios. The NH$_3$ yield rate and FE of 80-Ni-N$_2$O$_2$/rGO were
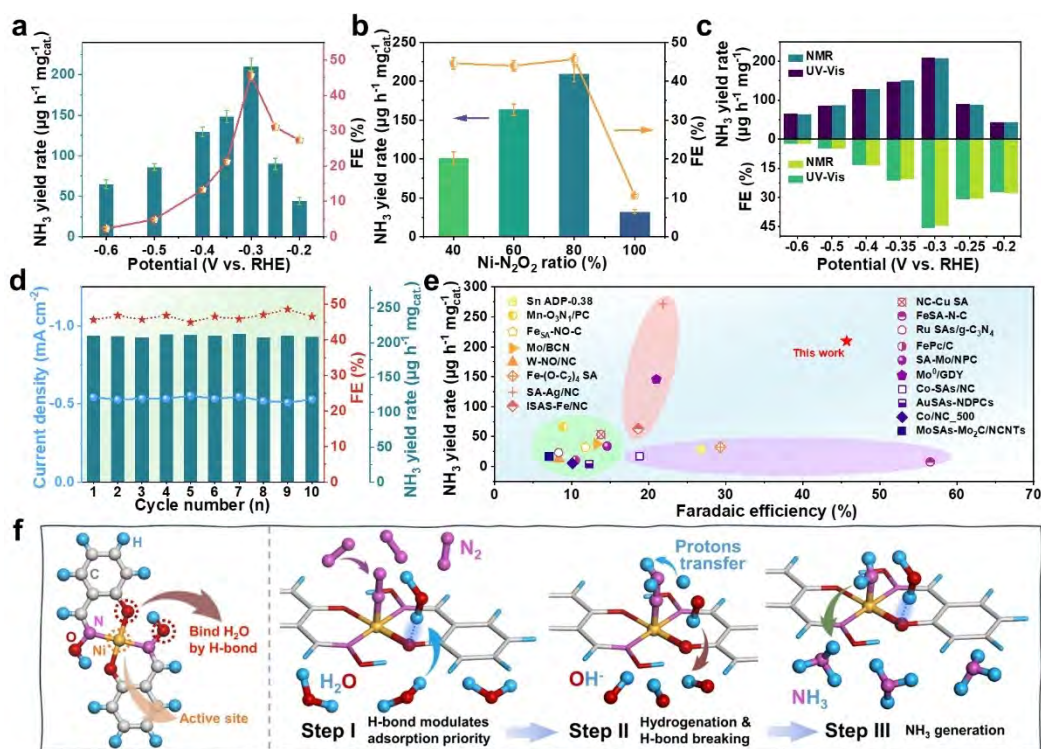

Figure 4. Performance of 80-Ni-N$_2$O$_2$/rGO. a) NH$_3$ yield rate and FE at each potential. b) NH$_3$ yield rate and FE of Ni-N$_2$O$_2$/rGO with various Ni-N$_2$O$_2$ contents at -0.3 V vs. RHE. c) Comparison of the NH$_3$ yield rate and FE by using UV-Vis and NMR methods over 80-Ni-N$_2$O$_2$/rGO. d) Stability of 80-Ni-N$_2$O$_2$/rGO at -0.3 V vs. RHE during a recycling test involving 10 cycles (2 h per cycle). e) NRR performance of 80-Ni-N$_2$O$_2$/rGO and other SA catalysts. Green zone: catalysts with both low yield rate and FE; Red zone: catalysts with high yield rate and low FE; Purple zone: catalysts with low yield rate and high FE. f) Proposed reaction mechanism of hydrogen-bond-regulated proton transfer during the NRR. The yellow, red, blue, pink, and white spheres represent Ni, O, H, N, and C, respectively. The abbreviations in e) are defined as follows: ADP, atomically dispersed protuberance; PC, porous carbon; NC, N-doped carbon; ISAS, isolated single atomic site; NPC and NDPCs, N-doped porous carbon; GDY, graphdiyne; and NCNTs, N-doped carbon nanotubes.

6.5 and 4.3 times higher than those of the MOHBF, respectively, which indicated the excellent activity and selectivity of 80-Ni-N_2O_2/rGO. In 80-Ni-N_2O_2/rGO, Ni-N_2O_2 molecules dispersed on the rGO substrate could fully utilize hydrogen bonds to bind H_2O molecules near Ni active sites to regulate proton behavior, thereby improving NRR selectivity. The remarkable NRR activity of Ni-N_2O_2 was also elucidated through DFT calculations. Nickel phthalocyanine (NiPc), a commonly used catalyst with a Ni–N_4 coordination structure, was employed as a control sample. The lengths of the bonds in N_2 molecules adsorbed on Ni sites in Ni-N_2O_2 and NiPc were found to be 1.141 Å and 1.130 Å, respectively, longer than that in free N_2 (1.120 Å), demonstrating the activated N_2 molecules (Figure S33).[6b,8] Moreover, Bader charge analysis (Figure S34) revealed that the number of electrons acquired by *N_2 was higher in Ni-N_2O_2 (0.31 e) than in NiPc (0.17 e) because of the unique local coordination structure of Ni-N_2O_2. After N_2 adsorption, the projected density of states (PDOS) for Ni sites contained an obvious energy-level overlap between the N orbital and the Ni orbital (Figure S35), which manifested a robust interaction between *N_2 and Ni sites within Ni-N_2O_2. As displayed in Figure S35c, the electrons of *N_2 entered the empty d orbital of Ni. Moreover, the $2\pi*$ orbital of *N_2 exhibited a notable shift to lower energy relative to the energy level for free N_2; this shift was due to the transfer of electrons from the Ni d orbital to the unoccupied $2\pi*$ orbital of N_2. This "accept-donate" mechanism strengthened the Ni–N bond while weakening the N≡N bond.[22]

Various controlled experiments were conducted to identify the source of N in the NH_3 produced through the NRR. A chronoamperometry test was conducted at the open-circuit potential with N_2 as the feed gas or at various potentials with Ar as the feed gas (Figure S36). No NH_3 was present in these post-electrolytes, which eliminated environmental interference. The ^1H nuclear magnetic resonance (NMR) spectra obtained after a chronoamperometry test in which $^{14}N_2$ or $^{15}N_2$ was employed as the feed gas revealed the characteristic peaks of triplet coupling for $^{14}NH_4^+$ (with a spacing of 52 Hz) and doublet coupling for $^{15}NH_4^+$ (with a spacing of 72 Hz), which corresponded well to the characteristic signals of standard samples (Figure S37a); thus, N_2 feed gas was the only source of N in the NRR for NH_3 generation.[23] In addition, quantitative NMR was performed using maleic acid as the internal standard (Figure S37). As shown in Figures 4c and S37d, there were negligible differences in the yield rate and FE for NH_3 generation obtained from the quantitative NMR and ultraviolet-visible (UV-Vis) spectroscopy methods; thus, the NH_3 generated in the NRR was confirmed to originate from N_2 feed gas. The electrocatalytic stability of 80-Ni-N_2O_2/rGO for the NRR was investigated by performing a chronoamperometry test at -0.3 V vs. RHE; the electrolyte was replaced every 2 h. As illustrated in Figure 4d, the NH_3 yield rate and FE did not change considerably during 10 consecutive cycles. Only a slight decrease in the current density was discovered in a 40-h chronoamperometry measurement (Figure S38), after which the 80-Ni-N_2O_2/rGO catalyst exhibited an essentially stable NH_3 yield rate and FE (Figure S39), and negligible

differences in the FTIR results (Figure S40), which indicated its excellent stability.

In addition, we summarized and compared the NRR performance of recently reported SA catalysts (Figure 4e, Table S3), which could be classified into three types that show: i) both low yield rate and FE (green zone); ii) high yield rate and low FE (red zone); iii) low yield rate and high FE (purple zone). This result suggested the leverage relationship between activity and selectivity in the NRR. Benefiting from the introduction of hydrogen bonds, 80-Ni-N_2O_2/rGO in our work modulated this relationship, thus achieving simultaneously enhanced activity and selectivity of NH_3 production.

Based on the aforementioned analyses, we propose a hydrogen-bond-regulated proton transfer process in the NRR. As illustrated in Figure 4f, this process involves three steps. Step I: hydrogen bonds modulate the adsorption priority between proton and N_2. The O atoms in Ni-O-C and N-O-H form hydrogen bonds with H_2O molecules at the solid-liquid interface, thus regulating the proton transfer process in the NRR. The unique bonding structure of Ni atoms creates a suitable electronic environment for adsorption, and the activity of H_2O molecules is inhibited by the hydrogen bonds. Overall, these features result in a lower barrier for N_2 molecule adsorption on Ni active sites and a simultaneous decrease in proton accessibility. The step is conductive to the designed catalyst's excellent activity and selectivity. Step II: hydrogenation reaction and hydrogen bond breaking. Subsequently, the remote hydrogen of the bound H_2O molecule participates in the hydrogenation of the NRR intermediate, and electrostatic interaction causes OH^- to be released; the released OH^- enters the PBS electrolyte and is then neutralized. This phenomenon was proven using different electrolytes. When 0.1 M PBS was used, the pH changed negligibly, whereas when 0.1 M K_2SO_4 was employed, the pH clearly increased over 3600 s (Figure S41). The hydrogen bond breaking noted in the DFT calculation also indicated OH^- release (Figure S42). Step III: NH_3 generation. Finally, after the continual repetition of steps I and II, the conversion from N_2 to NH_3 is complete.

In situ ATR-FTIR spectroscopy was adopted to explore possible intermediates in the NRR. As shown in Figures 5a–d, within the test potential range, distinct signals corresponding to O–H stretching and bending were obtained at 3450 and 1643 cm^{-1}, respectively. In addition, characteristic peaks of N=N stretching and N–H bending were found at 2071 and 1460 cm^{-1}, respectively. Notably, the intensity of these bands achieved the highest intensity at -0.3 V vs. RHE; this result agreed favorably with the NH_3 yield rate results for 80-Ni-N_2O_2/rGO. Moreover, the Ni–H peak located at 1986 cm^{-1} exhibited an increase in intensity and a negative shift with decreasing potential, which agrees with previous studies.[24] In the ATR-FTIR test in which Ar was used as the feed gas, no characteristic peaks corresponding to N=N stretching or N–H bending were obtained. In Ar- and N_2-saturated electrolytes, hydrogen bonds interfered with the direct adsorption of hydrogen on Ni. However, the intensity of the Ni–H signal under the N_2 condition was considerably lower than that under the Ar condition, and a N=N peak was
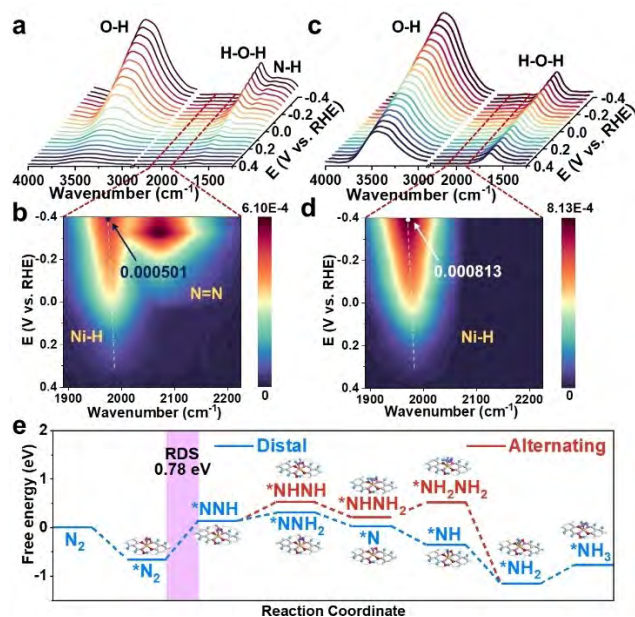
Figure 5. In situ ATR-FTIR spectroscopy and DFT calculations. a–d) In situ ATR-FTIR spectroscopy results of 80-Ni-N_2O_2/rGO in a) N_2-saturated and c) Ar-saturated electrolyte, and b,d) corresponding contour maps of the selected part in a,c). e) Free energy diagram in the NRR process and the corresponding adsorption configurations in associative distal and associative alternating pathways. The yellow, red, blue, pink, and white spheres represent Ni, O, H, N, and C, respectively.

discernible, indicating the excellent NRR activity of 80-Ni-N_2O_2/rGO. More importantly, hydrogen bonds could modulate site adsorption priority by binding H_2O molecules around Ni sites to improve selectivity. Online differential electrochemical mass spectrometry (DEMS) was employed to study the electrochemical NRR and investigate its intermediates and products.[25] Figure S43 shows the DEMS results obtained for 80-Ni-N_2O_2/rGO at −0.3 V vs. RHE in N_2-saturated electrolyte. No signal was obtained at mass-to-charge ratios (m/z) of 27, 30, 31, or 33 in comparison with the standard mass spectra depicted in Figure S44; thus, no fragments of N_2H_4 were obtained, as confirmed using the Watt-Chrisp method (Figure S30). Consequently, the distinctive signal at m/z = 15 proved the generation of NH_3. Furthermore, Figure S45a suggests that the ion current of NH_3 at m/z = 17 increased with a decrease in the potential and peaked at a potential of −0.3 V vs. RHE, which is in accordance with the NH_3 yield rate results shown in Figure 4a. Finally, Figure S45b indicates that the ion current was stable during the NRR. No signal was obtained when a potential was not applied, which reconfirmed that N_2 feed gas was the source of the NH_3 generated in the NRR.

DFT calculations were used to investigate the reaction pathway. The differential charge density distributions (Figure S46) revealed a notable interaction between the distal N of the N_2 molecule adsorbed on the Ni site and the hydrogen atom within the H_2O molecule. We constructed a free energy diagram to delve deeper into the NRR. The two primary pathways were studied, namely associative distal

and associative alternating routes (Figures S47 and S48). Figure 5e indicates that the rate-determining step (RDS) in both routes is *NN→*NNH (0.78 eV). In the processes involved in the transformations from *NNH to *NHNH and from *NHNH$_2$ to *NH$_2$NH$_2$, the associative alternating pathway demands more energy than the associative distal pathway does. Based on these results, we concluded that the NRR predominantly follows the associative distal pathway.

Conclusion

In summary, to modulate the leverage relationship between activity and selectivity in the NRR, we designed a novel molecular catalyst based on the MOHBF, namely Ni-N_2O_2/rGO. This catalyst can bind H_2O molecules through hydrogen bonds, thus reducing the activity of H_2O molecules and modulating the priority of adsorption for N_2 molecules versus protons. Ni SA sites coordinated by N/O atoms with a suitable surrounding electron environment ensure high activity. Therefore, Ni-N_2O_2/rGO can simultaneously achieve high selectivity and activity, modulating the leverage relationship. The NRR was found to occur through the following steps in sequence: N_2 molecules were adsorbed and activated on highly active Ni sites, while H_2O molecules were adsorbed through hydrogen bonds, followed by the participation of distal protons in bound H_2O molecules in the hydrogenation reaction, and eventually, NH_3 was generated. The as-prepared Ni-N_2O_2/rGO achieved a favorable NH_3 yield rate of 209.7 $\mu g\,h^{-1}\,mg_{cat.}^{-1}$ and an FE of 45.7%, outperforming previously reported SA NRR catalysts. This novel catalyst design strategy is a promising approach for simultaneously improving the yield and FE of catalytic reactions involving the hydrogenation process.

Conflict of Interest

The authors declare no conflict of interest.

Data Availability Statement

The data that support the findings of this study are available from the corresponding author upon reasonable request.

[1] a) P. Li, R. Li, Y. Liu, M. Xie, Z. Jin, G. Yu, *J. Am. Chem. Soc.*
2023, *145*, 6471–6479; b) X. Zhang, Y. Lyu, H. Zhou, J. Zheng,
A. Huang, J. Ding, C. Xie, R. De Marco, N. Tsud, V.
Kalinovych, S. P. Jiang, L. Dai, S. Wang, *Adv. Mater.* **2023**, *35*,
2211894; c) R. Zhang, C. Li, H. Cui, Y. Wang, S. Zhang, P. Li,
Y. Hou, Y. Guo, G. Liang, Z. Huang, C. Peng, C. Zhi, *Nat.
Commun.* **2023**, *14*, 8036.

[2] a) S. Liu, T. Qian, M. Wang, H. Ji, X. Shen, C. Wang, C. Yan,
Nat. Catal. **2021**, *4*, 322–331; b) L. Li, C. Tang, X. Cui, Y.
Zheng, X. Wang, H. Xu, S. Zhang, T. Shao, K. Davey, S. Z.
Qiao, *Angew. Chem.* **2021**, *133*, 14250–14256.

[3] a) H. Zhong, M. Wang, M. Ghorbani-Asl, J. Zhang, K. H. Ly,
Z. Liao, G. Chen, Y. Wei, B. P. Biswal, E. Zschech, I. M.
Weidinger, A. V. Krasheninnikov, R. Dong, X. Feng, *J. Am.
Chem. Soc.* **2021**, *143*, 19992–20000; b) S. Liu, M. Wang, Y. He,
Q. Cheng, H. Ji, Y. Huan, X. Shen, X. Zhou, T. Qian, C. Yan,
Adv. Mater. **2023**, *35*, 2303703; c) D. Chen, S. Zhang, D. Yin,
W. Li, X. Bu, Q. Quan, Z. Lai, W. Wang, Y. Meng, C. Liu, S.
Yip, F.-R. Chen, C. Zhi, J. C. Ho, *Adv. Energy Mater.* **2023**, *13*,
2203201.

[4] a) C. Chen, H. Jin, P. Wang, X. Sun, M. Jaroniec, Y. Zheng, S.-
Z. Qiao, *Chem. Soc. Rev.* **2024**, *53*, 2022–2055; b) H.-L. Du, M.
Chatti, R. Y. Hodgetts, P. V. Cherepanov, C. K. Nguyen, K.
Matuszek, D. R. MacFarlane, A. N. Simonov, *Nature* **2022**, *609*,
722–727.

[5] a) Z. Fang, P. Wu, Y. Qian, G. Yu, *Angew. Chem.* **2021**, *133*,
4321–4327; b) Y. Li, Y. Ji, Y. Zhao, J. Chen, S. Zheng, X. Sang,
B. Yang, Z. Li, Z. Lei, Z. Wen, X. Feng, Y. Hou, *Adv. Mater.*
2022, *34*, 2202240.

[6] a) L. Zhang, H. Zhou, X. Yang, S. Zhang, H. Zhang, X. Yang,
X. Su, J. Zhang, Z. Lin, *Angew. Chem. Int. Ed.* **2023**, *62*,
e202217473; b) Y. Kong, Y. Li, X. Sang, B. Yang, Z. Li, S.
Zheng, Q. Zhang, S. Yao, X. Yang, L. Lei, S. Zhou, G. Wu, Y.
Hou, *Adv. Mater.* **2022**, *34*, 2103548; c) L. Wen, K. Sun, X. Liu,
W. Yang, L. Li, H. L. Jiang, *Adv. Mater.* **2023**, *35*, 2210669.

[7] S. Qiang, F. Wu, J. Yu, Y. T. Liu, B. Ding, *Angew. Chem. Int.
Ed.* **2023**, *62*, e202217265.

[8] Y. Gu, B. Xi, W. Tian, H. Zhang, Q. Fu, S. Xiong, *Adv. Mater.*
2021, *33*, 2100429.

[9] a) B. H. Suryanto, K. Matuszek, J. Choi, R. Y. Hodgetts, H.-L.
Du, J. M. Bakker, C. S. Kang, P. V. Cherepanov, A. N.
Simonov, D. R. MacFarlane, *Science* **2021**, *372*, 1187–1191;
b) S. Zhang, D. Chen, Y. Guo, R. Zhang, Y. Zhao, Z. Huang,
J. Fan, J. C. Ho, C. Zhi, *Mater. Today* **2023**, *66*, 17–25.

[10] Y.-C. Hao, Y. Guo, L.-W. Chen, M. Shu, X.-Y. Wang, T.-A.
Bu, W.-Y. Gao, N. Zhang, X. Su, X. Feng, J.-W. Zhou, B.
Wang, C.-W. Hu, A.-X. Yin, R. Si, Y.-W. Zhang, C.-H. Yan,
Nat. Catal. **2019**, *2*, 448–456.

[11] a) L. Shi, S. Bi, Y. Qi, R. He, K. Ren, L. Zheng, J. Wang, G.
Ning, J. Ye, *ACS Catal.* **2022**, *12*, 7655–7663; b) Z. Qi, Y. Zhou,
R. Guan, Y. Fu, J. B. Baek, *Adv. Mater.* **2023**, *35*, 2210575;

c) X. Li, W. Xu, L. Q. Le, S. Chen, L. Song, T. S. Choksi, X.
Wang, *Chem Catal.* **2023**, *3*, 100724.

[12] a) X. Lin, Y. Wang, X. Chang, S. Zhen, Z. J. Zhao, J. Gong,
Angew. Chem. **2023**, *135*, e202300122; b) Y. Ni, L. Lin, Y.
Shang, L. Luo, L. Wang, Y. Lu, Y. Li, Z. Yan, K. Zhang, F.
Cheng, J. Chen, *Angew. Chem. Int. Ed.* **2021**, *60*, 16937–16941.

[13] a) Y. Fang, Y. Fan, K. Xie, W. Ge, Y. Zhu, Z. Qi, Z. Song, H.
Jiang, C. Li, *Angew. Chem. Int. Ed.* **2023**, *62*, e202304413; b) T.
Wang, Z. Tian, Z. You, Z. Li, H. Cheng, W. Li, Y. Yang, Y.
Zhou, Q. Zhong, Y. Lai, *Energy Storage Mater.* **2022**, *45*, 24–
32.

[14] a) C. Xiao, L. Cheng, Y. Zhu, G. Wang, L. Chen, Y. Wang, R.
Chen, Y. Li, C. Li, *Angew. Chem. Int. Ed.* **2022**, *61*,
e202206544; b) Y. Zhang, L. Jiao, W. Yang, C. Xie, H. L. Jiang,
Angew. Chem. Int. Ed. **2021**, *60*, 7607–7611.

[15] a) K. Fan, J. Li, Y. Xu, C. Fu, Y. Chen, C. Zhang, G. Zhang, J.
Ma, T. Zhai, C. Wang, *J. Am. Chem. Soc.* **2023**, *145*, 12682–
12690; b) Q. Q. Sun, T. Sun, J. Y. Du, K. Li, H. M. Xie, G.
Huang, X. B. Zhang, *Adv. Mater.* **2023**, *35*, 2301088; c) Y.
Chen, M. Tang, Y. Wu, X. Su, X. Li, S. Xu, S. Zhuo, J. Ma, D.
Yuan, C. Wang, W. Hu, *Angew. Chem. Int. Ed.* **2019**, *58*,
14731–14739; d) J. Gu, H. Fan, C. Li, J. Caro, H. Meng, *Angew.
Chem.* **2019**, *131*, 5351–5355.

[16] Z. Song, L. Miao, H. Duan, L. Ruhlmann, Y. Lv, D. Zhu, L.
Li, L. Gan, M. Liu, *Angew. Chem.* **2022**, *134*, e202208821.

[17] N. Cao, Z. Chen, K. Zang, J. Xu, J. Zhong, J. Luo, X. Xu, G.
Zheng, *Nat. Commun.* **2019**, *10*, 2877.

[18] X. Zhu, H. Huang, H. Zhang, Y. Zhang, P. Shi, K. Qu, S.-B.
Cheng, A.-L. Wang, Q. Lu, *ACS Appl. Mater. Interfaces* **2022**,
14, 32176–32182.

[19] H. Zhang, F. Wan, X. Li, X. Chen, S. Xiong, B. Xi, *Adv. Funct.
Mater.* **2023**, *33*, 2306340.

[20] a) R. Zhang, Y. Guo, S. Zhang, D. Chen, Y. Zhao, Z. Huang,
L. Ma, P. Li, Q. Yang, G. Liang, C. Zhi, *Adv. Energy Mater.*
2022, *12*, 2103872; b) X. Li, S. Tang, S. Dou, H. J. Fan, T. S.
Choksi, X. Wang, *Adv. Mater.* **2022**, *34*, 2104891.

[21] S. Zhang, D. Chen, P. Chen, R. Zhang, Y. Hou, Y. Guo, P. Li,
X. Liang, T. Xing, J. Chen, Y. Zhao, Z. Huang, D. Lei, C. Zhi,
Adv. Mater. **2024**, *36*, 2310776.

[22] J. Chen, Q. Ma, M. Li, D. Chao, L. Huang, W. Wu, Y. Fang, S.
Dong, *Nat. Commun.* **2021**, *12*, 3375.

[23] Y. Guo, J. Gu, R. Zhang, S. Zhang, Z. Li, Y. Zhao, Z. Huang,
J. Fan, Z. Chen, C. Zhi, *Adv. Energy Mater.* **2021**, *11*, 2101699.

[24] a) S. Zhu, X. Qin, F. Xiao, S. Yang, Y. Xu, Z. Tan, J. Li, J.
Yan, Q. Chen, M. Chen, M. Shao, *Nat. Catal.* **2021**, *4*, 711–718;
b) J.-Y. Fang, Q.-Z. Zheng, Y.-Y. Lou, K.-M. Zhao, S.-N. Hu,
G. Li, O. Akdim, X.-Y. Huang, S.-G. Sun, *Nat. Commun.* **2022**,
13, 7899; c) Y. Yao, S. Zhu, H. Wang, H. Li, M. Shao, *J. Am.
Chem. Soc.* **2018**, *140*, 1496–1501.

[25] D. Yao, C. Tang, L. Li, B. Xia, A. Vasileff, H. Jin, Y. Zhang,
S. Z. Qiao, *Adv. Energy Mater.* **2020**, *10*, 2001289.